

## THE TRACE OF THE CNO CYCLE IN THE RING NEBULA NGC 6888\*

A. MESA-DELGADO<sup>1</sup> †

<sup>1</sup>Instituto de Astrofísica, Facultad de Física, Pontificia Universidad Católica de Chile, Av. Vicuña Mackenna 4860, 782-0436 Macul, Santiago, Chile

C. ESTEBAN<sup>2,3</sup>, J. GARCÍA-ROJAS<sup>2,3</sup>,

<sup>2</sup>Instituto de Astrofísica de Canarias, E-38200 La Laguna, Tenerife, Spain and

<sup>3</sup>Departamento de Astrofísica. Universidad de La Laguna, E38205 La Laguna, Tenerife, Spain

J. REYES-PÉREZ<sup>4</sup>, C. MORISSET<sup>4</sup>

<sup>4</sup>Instituto de Astronomía, Universidad Nacional Autónoma de México, Apdo. Postal 70264, Méx. D. F., 04510 México

AND F. BRESOLIN<sup>5</sup>

<sup>5</sup>Institute for Astronomy, 2680 Woodlawn Drive, Honolulu, HI 96822, USA

*The Astrophysical Journal*, XXX:XXXX–XXXX, 2014 XX XX

### ABSTRACT

We present new results on the chemical composition of the Galactic ring nebula NGC 6888 surrounding the WN6(h) star WR136. The data are based on deep spectroscopical observations taken with the High Dispersion Spectrograph at the 8.2 m Subaru Telescope. The spectra cover the optical range from 3700 to 7400 Å. The effect of the CNO cycle is well identified in the abundances of He, N, and O, while elements not involved in the synthesis such as Ar, S, and Fe present values consistent with the solar vicinity and the ambient gas. The major achievement of this work is the first detection of the faint C II  $\lambda$ 4267 recombination line in a Wolf-Rayet nebula. This allows to estimate the C abundance in NGC 6888 and therefore investigate for the first time the trace of the CNO cycle in a ring nebula around a Wolf-Rayet star. Although the detection of the C II line has a low signal-to-noise ratio, the C abundance seems to be higher than the predictions of recent stellar evolution models of massive stars. The Ne abundance also show a puzzling pattern with an abundance of about 0.5 dex lower than the solar vicinity, which may be related to the action of the NeNa cycle. Attending to the constraints imposed by the dynamical timescale and the He/H and N/O ratios of the nebula, the comparison with stellar evolution models indicates that the initial mass of the stellar progenitor of NGC 6888 is between 25  $M_{\odot}$  and 40  $M_{\odot}$ .

*Subject headings:* ISM: abundances – ISM: bubbles – ISM: individual: NGC 6888 – stars: Wolf-Rayet – stars: WR136

### 1. INTRODUCTION

Massive stars ( $\geq 20 M_{\odot}$ ) play an important role in the chemical evolution and chemical enrichment of galaxies since they are major sources of metals in the Universe. They dominate the feedback to the local circumstellar environment during their relatively short lifetimes, between 3 and 10 million years (Ekström et al. 2012). Through the emission of ionizing photons, the action of their strong stellar winds and their death as core-collapse supernova, massive stars interact with their surroundings injecting great amounts of radiation, mass and mechanical energy. An obvious manifestation of these interactions is the production of ring nebulae, i.e. filamentary shells that are found around evolved massive stars, especially Wolf-Rayet (WR) stars (e.g. Miller & Chu 1993; Marston et al. 1994a,b; Dopita et al. 1994; Marston 1997; van der Hucht 2001). Actually, WR features revealing the interaction between massive stars and the interstellar medium (ISM) are often observed in the integrated spectrum of star-forming galaxies (e.g. Schaerer et al. 1999; López-Sánchez & Esteban 2009, 2010).

The true nature of ring nebulae was first pointed out by Johnson & Hogg (1965) in the study of the Galactic objects

NGC 6888 and NGC 2359. Today, their origin and evolution are understood in the framework of massive star evolution (e.g. Garcia-Segura et al. 1996a,b; Freyer et al. 2003, 2006; van Marle et al. 2005, 2007). It is well established that ring nebulae are interstellar bubbles of ionized gas that have swept up the surrounding medium during the mass-loss episodes of their central massive stars (Weaver et al. 1977). The mass-loss episodes are simply the different phases of the stellar wind, which is especially powerful during the post-main sequence stages, playing an active role in the evolution of massive stars (Vink et al. 2001, 2011b).

The interaction between the stellar wind and the circumstellar medium can produce ring nebulae with distinct characteristics. They will depend on the properties of the surroundings and of the stellar progenitor as well as its evolutive stage. Low-dense and hot interstellar bubbles are produced by the fast stellar winds of massive stars along the main sequence (MS) stage. They have been observed in the optical range (e.g. Marston 1997; Stock & Barlow 2010), at 21 cm (e.g. Cappa et al. 2005) and at 24  $\mu\text{m}$  (e.g. Kraemer et al. 2010). These bubbles can be partially filled by the dense and slow stellar wind that operates during the phases of red supergiant (RSG) or luminous blue variable (LBV), depending on the initial mass of the progenitor. With the beginning of the WR phase, the material of the RSG wind is blown by the strong stellar

†E-mail: amesad@astro.puc.cl

\* Based on data collected at Subaru Telescope, which is operated by the National Astronomical Observatory of Japan.

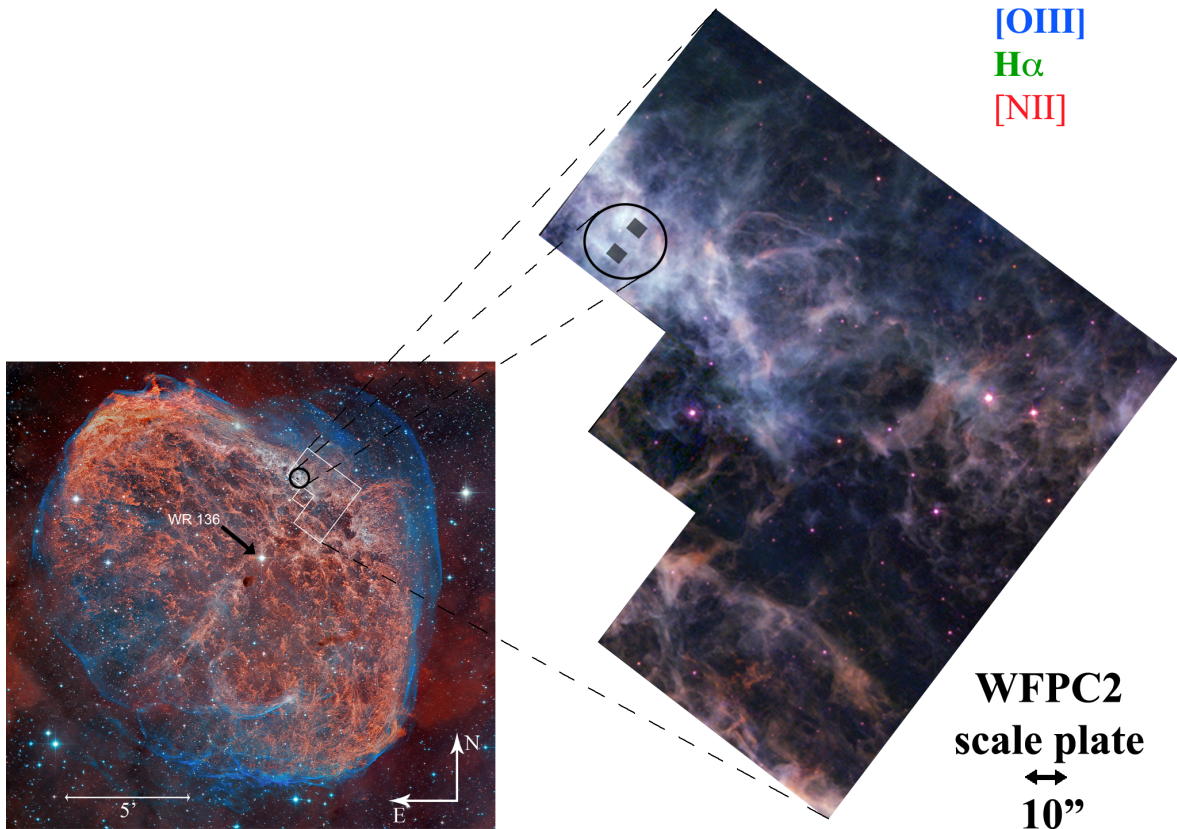


FIG. 1.— The large extension of NGC 6888 is shown in the image obtained with the Wide Field Camera at the Isaac Newton Telescope (left, image release at <http://www.ing.iac.es/PR/press/NGC6888.html>). The image combines  $H\alpha$  emission (red channel), 25%  $H\alpha$  and 75% [O III] emissions (green channel), and [O III] emission (blue channel). The zoomed field to the right corresponds to an image observed with the Wide Field Planetary Camera 2 (WFPC2) on board the *Hubble Space Telescope* by the 8568 program. The image represents our own combination of the filters F502N ([O III]  $\lambda$ 5007, blue), F656N ( $H\alpha$ , green), and F658N ([N II]  $\lambda$ 6583, red). The location of the slits observed with HDS are shown on the WFPC2 image. The slit covering the blue range is the one at the northwest and that corresponding to the red range is at the southeast. The slits were orientated with a position angle of  $50^\circ$  and cover an area of  $3'' \times 4''$ .

wind and, finally, compressed into long filaments after the WR shell reaches the RSG shell. According to the calculations of van Marle et al. (2005), the remaining shell will dissipate over  $\sim 80,000$  years after the beginning of the WR phase. In the literature, excellent works review in detail the evolutionary tracks of massive stars and the production of ring nebulae through the different stellar stages (e.g. Arthur 2007; Freyer et al. 2006; Toalá & Arthur 2011).

An interesting group of ring nebulae is that presenting chemical traces of processed stellar material; the ejected and wind-blown types as defined in the classification of Chu (1981), recently reviewed by Stock & Barlow (2010). These particular nebulae are thought to be blown by the stellar progenitors of long-duration  $\gamma$ -ray bursts (e.g. Vink et al. 2011a; Gräfener et al. 2012). They are powerful channels of information, directly connected to previous evolutionary phases. The enrichment process involves the transport of nucleosynthetic products from the stellar core to the outer layers, expelled in the post-MS stages. Thus, the study of their chemical abundances provides a unique opportunity to probe the stellar nucleosynthesis yield, an essential ingredient for our understanding of the chemical evolution of massive stars. From the analysis of He, N, O and Ne abundances, observational studies (e.g. Esteban et al. 1990, 1992; Stock et al. 2011) have shown that ring nebulae containing stellar ejecta have overabundances of He and N, and a deficiency of O. The results indicate that a substantial fraction of O has been transformed into N in the stellar interior via the activation of the ON cycle. The enrichment pattern is consistent with the stellar nucleosynthesis of the H-burning

through the CNO cycle, the main nuclear reactions working in massive stars along the MS. However, the lack of reliable determinations of C abundances in any ring nebulae has hindered for decades the full knowledge of the CNO cycle trace.

NGC 6888 is a prototype example of Galactic ring nebulae: a wind-blown bubble presenting clear traces of stellar nucleosynthetic products (e.g. Kwitter 1981; Esteban & Vilchez 1992). A direct indication that NGC 6888 is a wind-blown bubble is the detection of X-ray emission in the bubble interior (e.g. Bochkarev 1988; Wrigge et al. 1994), produced by the interaction between the WR wind and the RSG material that heats up the gas at  $\sim 10^6$  K (Weaver et al. 1977). Near the geometrical center of the nebula is located the stellar progenitor and ionizing source, the star HD 192163 (WR136; van der Hucht 2001), a WN6(h)-type star in the WR phase with a mass of about  $15 M_\odot$  (Hamann et al. 2006). NGC 6888 is the best-studied nebula of its class thanks to its proximity ( $1.45 \pm 0.50$  kpc; van Leeuwen 2007) and its large extension of about  $8 \times 5$  pc<sup>2</sup> ( $18' \times 12'$  on the sky). It resembles an almost complete ellipse, populated of filamentary structures of ionized gas. The mass of these structures amounts to  $3.5$ – $5 M_\odot$  (Wendker et al. 1975; Kwitter 1981; Marston & Meaburn 1988), with a typical electron density of about  $300$  cm<sup>-3</sup> (e.g. Esteban & Vilchez 1992; Fernández-Martín et al. 2012). The filaments mainly emit in [N II] and  $H\alpha$ , while they are surrounded by a highly-ionized, thin skin of material emitting in [O III] (Mitra 1991; Gruendl et al. 2000; Moore et al. 2000). The [O III] layer represents the boundary between the MS bubble and the WR shell; instead, the filaments are RSG wind material,

possible mixed with the WR wind, compressed after the WR shell collides with the RSG shell (e.g. Kwitter 1981; Esteban & Vilchez 1992; Moore et al. 2000). The gas kinematics have been studied in the past by several authors (e.g. Chu 1988; Marston & Meaburn 1988), showing that NGC 6888 expands on average at  $80 \text{ km s}^{-1}$ , though the velocity field is complex with variations ranging from  $55$  to  $110 \text{ km s}^{-1}$  (Lozinskaya 1970). From these velocities, the dynamical age of the WR shell is estimated in  $\sim 30,000$  years, varying between  $20,000$  and  $40,000$  years (see Freyer et al. 2006).

In this paper, we review the CNO cycle trace in the chemical composition of the Galactic ring nebula NGC 6888, especially focusing on the determination of the total C abundance as derived from the faint C II  $\lambda 4267$  recombination line. In §2 the observations are presented. A description of our spectrum as well as the methodology used in the line measurements and in the extinction correction can be found in §3. Physical conditions, chemical abundances and their calculations are found in §4. In §5 the abundance pattern found in NGC 6888 is compared with those expected by the CNO cycle and the predictions by stellar evolution models. In §6, the results are discussed in the light of previous ones for other similar objects and the future perspectives of exploring the C content in ring nebulae around massive stars. Finally, in §7 we summarize our main conclusions.

## 2. OBSERVATIONS AND DATA REDUCTION

NGC 6888 was observed on 2009 September 14 at Mauna Kea Observatory (Hawai'i), using the 8.2 m Subaru Telescope with the High Dispersion Spectrograph (HDS, Noguchi et al. 2002). We used the blue and red cross dispersers with different inclination angles of the echelle grating in order to have an almost complete coverage of the optical range. The spectra taken with the blue cross disperser cover from  $3667$  to  $5301 \text{ \AA}$  with a gap between CCDs extending from  $4436$  to  $4565 \text{ \AA}$ . In the case of the spectra taken with the red cross disperser, they cover from  $4777$  to  $7400 \text{ \AA}$  with a gap between  $5993$  and  $6237 \text{ \AA}$ . For all spectra we used a slit length of  $6''$  and a width of  $3''$ , leading to a spectral resolution of  $R \sim 12,000$ . We take three consecutive exposures of  $300$  and  $1800$  seconds for the spectra obtained with the red and blue cross dispersers, respectively. These individual exposures were added to obtain the final spectra. The slit was located in a bright zone of the nebula located at the northwest of the ionizing WR star (see Fig. 1) and with a position angle of  $50^\circ$ . The atmospheric dispersion corrector (ADC) was used to keep the same observed region within the slit regardless of the air mass value. It was discovered while the data were being analyzed that the red and blue pointings were spatially offset ( $\sim 10''$ ; see Fig. 1), an effect we will discuss further in §3.2. Inspecting the headers of the data files we found that the mean coordinates of the three spectra of the blue range are  $\alpha = 20^{\text{h}}11^{\text{m}}58^{\text{s}}.9$  and  $\delta = +38^\circ 24' 33''.3$  (J2000.0); and of those of the red range:  $\alpha = 20^{\text{h}}11^{\text{m}}59^{\text{s}}.3$  and  $\delta = +38^\circ 24' 26''.8$  (J2000.0). Unfortunately, this mismatch was unnoticed during the observations.

The spectra were reduced using the IRAF<sup>2</sup> echelle reduction package, following the standard procedure of bias subtraction, aperture extraction, flatfielding, background subtraction, wavelength calibration, and flux calibration. A total area of  $3'' \times 4''.4$  was extracted to analyze the nebular emission. The

<sup>2</sup> IRAF is distributed by NOAO, which is operated by AURA, under cooperative agreement with NSF.

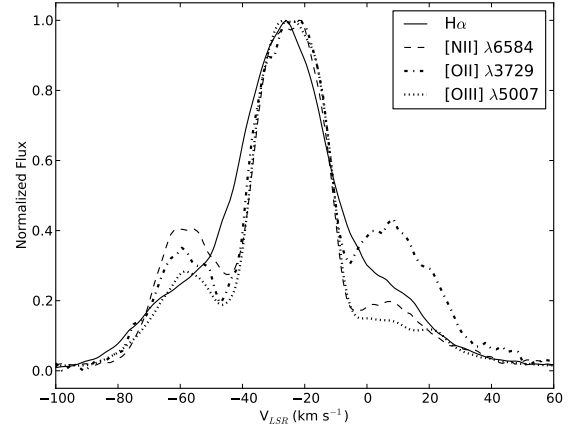


FIG. 2.— Velocity profiles of selected emission lines:  $H\alpha$  (solid line),  $[\text{N II}] \lambda 6584$  (dashed line),  $[\text{O II}] \lambda 3729$  (dotted-dashed line) and  $[\text{O III}] \lambda 5007$  (dotted line). Three kinematical components are detected at systemic velocities  $V_{\text{LSR}}$  of about  $-60$ ,  $-25$  and  $+12 \text{ km s}^{-1}$ .

standard stars BD  $+28^\circ 4211$  and Feige 110 (Oke 1990) were observed to perform the flux calibration, whose uncertainty has been estimated to be of the order of  $3\text{--}5\%$ .

## 3. EMISSION LINES AND REDDENING CORRECTION

### 3.1. Kinematical components

The spectral resolution provided by HDS allowed us to detect three kinematical components in most emission lines. The velocity profiles of  $H\alpha$ ,  $[\text{N II}] \lambda 6584$ ,  $[\text{O II}] \lambda 3729$  and  $[\text{O III}] \lambda 5007$  are presented in Fig. 2. The three components are clearly seen at systemic velocities  $V_{\text{LSR}}$  of about  $-60$ ,  $-25$  and  $+12 \text{ km s}^{-1}$ . Though the red and blue ranges were observed at different positions on the northwest field, it should be noted that we detected the three kinematical components at the same velocities in both slit positions. The different width of the emission lines can be also seen in Fig. 2.  $H\alpha$  is clearly wider due to its larger thermal broadening on account of its lower atomic weight.

In previous studies, the red-shifted component detected at  $+12 \text{ km s}^{-1}$  in NGC 6888 has been usually associated with ambient emission from interstellar material, probably ionized by the Cygnus OB1 association (Lozinskaya 1970; Treffers & Chu 1982; Marston & Meaburn 1988; Chu 1988). The two blue-shifted components correspond to nebular material at different velocities in an approaching shell. Receding kinematical components of the shell were not detected in our spectra. According to Treffers & Chu (1982), that component is more prominent in the southwest part of the nebula. The absence of emission from the red-shifted component has been reported in previous works (Lozinskaya 1970; Johnson & Songsathaporn 1981) and it can be associated with the presence of complex velocity structures near the edge of the shell, which is well populated of high-density knots (see Fig. 1). Using high-resolution Fabry-Pérot observations with a resolution of  $6.4 \text{ km s}^{-1}$ , Johnson & Songsathaporn (1981) mapped the  $[\text{N II}]$  velocity structure in NGC 6888 finding the existence of three blue-shifted kinematical components in most of their positions at the edge of the nebula. Their positions 19 and 21 are very close to our slit positions with velocities  $V_{\text{LSR}}$  of about  $(-57, -31, -4)$ , and  $(-35, -16, -1) \text{ km s}^{-1}$ , respectively, which are in agreement with our determinations. Our blue-shifted components may correspond to unresolved blends of the velocity

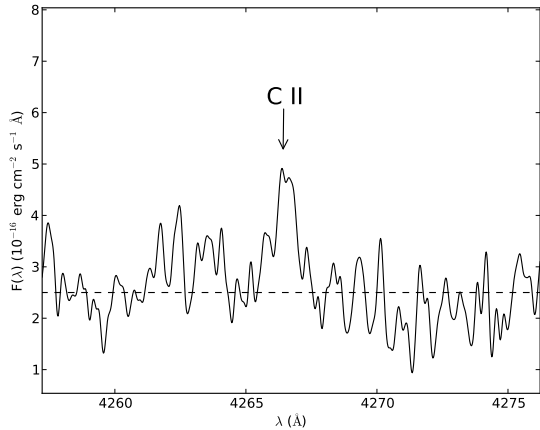


FIG. 3.— Section of the echelle spectrum showing the C II  $\lambda 4267$  emission line, which is the first detection of this feature in NGC 6888. The dashed line corresponds to the average local continuum used to measure this line.

systems detected by these authors.

### 3.2. Line measurements

Making use of the `SPLIT` routine of `IRAF`, line fluxes were measured applying a multiple Gaussian fitting over the average local continuum. Errors in the flux measurements were estimated from multiple measurements considering the continuum noise for all lines. The blend of He I  $\lambda 3889$  and H8 was difficult to resolve. Only the He I and H8 emissions associated with the kinematical components at  $-60$  and  $+12$  km s $^{-1}$ , respectively, were well isolated. We managed to estimate the fluxes of the three components of those lines from flux measurements of the blends and considering the theoretical H8/H $\beta$  ratio.

Integrated flux measurements were also considered for faint and single emission lines. In particular, this was the case of the recombination line C II  $\lambda 4267$ , which represents the first detection of this feature in NGC 6888. The line was detected with a signal of  $1.6\sigma$  over the continuum. For a proper measurement of this line, a Gaussian filter was applied to smooth the noise of the local continuum resulting as it is shown in Fig. 3.

Three bright emission lines are presented in the common range of the blue and red spectra: H $\beta$  and [O III]  $\lambda\lambda 4959, 5007$ . We noticed a disagreement in the fluxes measured of those lines in both spectral ranges, thus confirming the pointing mismatch that we noted after the observations (see §2 and Fig. 1). The flux measurements in red range were on average 34% lower than those in the blue one for the three kinematical components. Considering these differences, each spectral range was separately analyzed to produce a final homogeneous set of line flux ratios rescaled to its respective H $\beta$ . Errors in the flux ratios were propagated from the H $\beta$  normalization.

### 3.3. Reddening correction

Observed line fluxes,  $F(\lambda)$ , are affected by reddening due to the presence of dust along the line of sight. Given a reference emission line (typically, H $\beta$ ), the reddening can be corrected through the usual expression:

$$\frac{I(\lambda)}{I(\text{H}\beta)} = \frac{F(\lambda)}{F(\text{H}\beta)} 10^{c(\text{H}\beta) \times [f(\lambda) - f(\text{H}\beta)]}, \quad (1)$$

where  $I(\lambda)$  represents the dereddened flux; the reddening coefficient,  $c(\text{H}\beta)$ , accounts for the amount of interstellar extinction at H $\beta$ ; and  $f(\lambda)$  is the adopted extinction curve. In our calculations, the reddening law  $f(\lambda)$  of Cardelli et al. (1989) was adopted using a ratio of total to selective extinction  $R_V = 3.1$ , the typical value of the diffuse interstellar medium. The extinction correction was calculated with `PYNEB` (Luridiana et al. 2012), an updated `PYTHON` version of the `NEBULAR` package of `IRAF`.

For each kinematical component, the extinction coefficient was determined by comparing the observed ratios of the available H I emission lines relative to H $\beta$  with the theoretical ones for the case B predicted by Storey & Hummer (1995), assuming an electron density  $n_e = 1000$  cm $^{-3}$  and an electron temperature  $T_e = 10,000$  K. Besides H $\beta$ , several H I lines of the Balmer series were detected: H $\alpha$ , H $\gamma$ , H $\delta$ , H7, H8, H9, H11 and H12. In the red range, the  $c(\text{H}\beta)$  was directly given by the H $\alpha$ /H $\beta$  ratio. In the blue range, the adopted  $c(\text{H}\beta)$  was calculated as the weighted average of individual  $c(\text{H}\beta)$  values. In all cases, H8 was not considered since it is blended with He I  $\lambda 3889$ . Also, H12 was discarded because its faintness only contributes to increase the error of the average extinction. H $\gamma$ , H $\delta$ , H7, H9, and H11 were used for both  $-25$  km s $^{-1}$  and combined blue-shifted components. In the fainter components, the  $c(\text{H}\beta)$  was calculated from the brighter lines: H $\delta$ , H7, and H9 for the  $-60$  km s $^{-1}$  component; and H $\gamma$ , H $\delta$ , and H7 for the red-shifted component. H $\gamma$  was discarded in the  $-60$  km s $^{-1}$  component due to the reasons that we comment below. The final errors were obtained summing quadratically the weighted error and the standard deviation. In both spectral ranges, the different kinematical components present similar values of the reddening coefficient of about 0.3-0.4 dex (see Table 1), in agreement with the typical ones found in other zones of the nebula (e.g. Kwitter 1981; Esteban & Vilchez 1992; Fernández-Martín et al. 2012).

During the extinction analysis, it was noted that the H $\gamma$ /H $\beta$  ratio always returned a  $c(\text{H}\beta)$  coefficient lower than the other ratios, especially in the case of the  $-60$  km s $^{-1}$  component. The raw data do not show any anomalous effect around the H $\gamma$  emission. The flux calibration and the combination of orders were also checked, leading us to the same results. We concluded that this behavior might be related to radiative-transfer problems (Osterbrock & Ferland 2006). These effects would alter the H $\alpha$ /H $\beta$  and H $\gamma$ /H $\beta$  ratios, returning discrepant reddening values. Anomalous behaviors of the  $c(\text{H}\beta)$  coefficient determined from different pairs of Balmer lines have been reported and investigated in previous works (e.g. Mesa-Delgado et al. 2009). Unfortunately, the dataset is not deep enough to explore this issue in NGC 6888 with the required accuracy.

In Table 1, we present –for each spectral range– the final list of line identifications (columns 1–3) as well as the dereddened flux ratios,  $F(\text{H}\beta)$ , and  $c(\text{H}\beta)$  coefficients for the kinematical components  $-60$  km s $^{-1}$  (column 4),  $-25$  km s $^{-1}$  (column 5) and  $+12$  km s $^{-1}$  (column 6). Additionally, we have included the line ratios associated with the sum of the two blue-shifted components, named as “Combined” in column 7. For those lines only detected at  $-25$  km s $^{-1}$ , we just assumed that the measured flux comes from the two blue-shifted components. As we will see in §4, these two kinematical components have very similar physical and chemical properties and, therefore, it is convenient to analyze their sum. The errors associated with the line ratios include the uncertainties in the flux measurement, the normalization, and the reddening correction, which were propagated from equation (1).

TABLE 1  
IDENTIFICATIONS AND DEREDDENED LINE RATIOS NORMALIZED TO  $I(\text{H}\beta) = 100$  FOR THE THREE KINEMATICAL COMPONENTS WITH VELOCITIES  $V_{\text{LSR}}$  OF  $-60$ ,  $-25$ , AND  $+12$   $\text{km s}^{-1}$  AS WELL AS FOR THE COMBINATION OF THE TWO BLUE-SHIFTED COMPONENTS (COMBINED).

$\lambda$ (Å)	Ion	Mult.	$I(\lambda)/I(\text{H}\beta)^a$			
			$-60$ $\text{km s}^{-1}$	$-25$ $\text{km s}^{-1}$	$+12$ $\text{km s}^{-1}$	Combined
Blue Range						
3726.03	[O II]	1F	30±4	21±1	38±8	22±2
3728.82	[O II]	1F	33±5	23±1	53±10	24±2
3750.15	H I	H12	...	2.5±0.9	...	2.1±0.8
3770.63	H I	H11	...	4.1±0.5	...	3.5±0.5
3797.63	[S III]	2F	...	4.9±0.8	...	4.2±0.7
3819.61	He I	22	...	2.1±0.6	...	1.8±0.5
3835.39	H I	H9	7±2	7.9±0.6	10±3	7.8±0.8
3868.75	[Ne III]	1F	22±3	16±1	17±7	17±2
3888.65	He I	2	16±3	8.7±0.9	4±1	10±1
3889.05	H I	H8	13±3	13±1	13±3	13±1
3964.73	He I	5	...	0.8±0.3	...	0.7±0.2
3967.46	[Ne III]	1F	3.9:	4.2±0.6	4.0:	4.1±0.6
3970.07	H I	H7	14±3	15±1	14±5	15±1
4026.21	He I	18	3.7:	3.7±0.6	5.1:	3.7±0.6
4101.74	H I	H $\delta$	26±3	26±1	25±4	26±2
4267.15	C II	6	...	0.8:	...	0.7:
4340.47	H I	H $\gamma$	55±4	49±2	49±6	50±3
4359.34	[Fe II]	7F	...	0.6±0.2	...	0.5±0.2
4363.21	[O III]	2F	1.5±0.6	1.5±0.5	...	1.5±0.5
4387.93	He I	51	0.9±0.5	1.1±0.2	...	1.1±0.2
4630.54	N II	5	...	0.6±0.2	...	0.5±0.2
4658.10	[Fe III]	3F	2.3±0.8	1.2±0.3	...	1.4±0.3
4713.14	He I	12	...	1.07:	...	0.91:
4861.33	H I	H $\beta$	100±3	100±1	100±3	100±1
4921.93	He I	48	1.8:	2.4±0.2	1.7:	2.3±0.1
4958.91	[O III]	1F	106±3	91±2	49±2	93±2
5006.84	[O III]	1F	310±10	268±4	141±7	274±5
5015.68	He I	4	4±1	4.5±0.1	3±1	4.4±0.2
	$F(\text{H}\beta)^b$		5.6±0.1	31.6±0.3	5.6±0.1	37.2±0.4
	$c(\text{H}\beta)$		0.34±0.15	0.28±0.08	0.33±0.22	0.30±0.13
Red Range						
4861.33	H I	H $\beta$	100±7	100±1	100±7	100±1
4958.91	[O III]	1F	89±6	75±1	38±3	77±1
5006.84	[O III]	1F	254±18	218±3	113±8	224±3
5875.64	He I	11	22±9	27±3	20±8	26±3
6548.03	[N II]	1F	60±6	41±1	29±3	44±1
6562.82	H I	H $\alpha$	285±29	285±6	285±29	285±6
6583.41	[N II]	1F	189±19	118±3	90±9	130±3
6678.15	He I	46	...	8.2±0.5	...	6.8±0.4
6716.47	[S II]	2F	4.9:	3.8:	...	4.0:
6730.85	[S II]	2F	...	4.6:	...	3.8:
7065.28	He I	10	...	3.2±0.4	...	2.6±0.3
7135.78	[Ar III]	1F	16±2	21±1	8±2	20±1
	$F(\text{H}\beta)^b$		2.0±0.1	10.6±0.1	2.1±0.1	12.6±0.1
	$c(\text{H}\beta)$		0.43±0.10	0.32±0.03	0.35±0.10	0.34±0.03

<sup>a</sup> Colons indicate an error equal or higher than 50%

<sup>b</sup> In units of  $10^{-15}$   $\text{erg cm}^{-2} \text{s}^{-1}$  on an extracted area of  $3'' \times 4''$ .

#### 4. CALCULATIONS AND RESULTS

##### 4.1. Physical conditions

Physical conditions were calculated with PYNEB in combination with the atomic data listed in Table 2.  $T_e$  and  $n_e$  were determined making use of the diagnostic ratios available in our spectrum: [S II]  $\lambda 6731/\lambda 6717$  and [O II]  $\lambda 3726/\lambda 3729$  to derive  $n_e$ ; and [O III]  $\lambda 4363/\lambda 5007$  to derive  $T_e$ . All diagnostic lines were detected for the central component at  $-25$   $\text{km s}^{-1}$ . The [S II]  $\lambda 6731$  and [O III]  $\lambda 4363$  diagnostic lines were not detected in the kinematical components at  $-60$   $\text{km s}^{-1}$  and  $+12$   $\text{km s}^{-1}$ , respectively. Uncertainties in the physical conditions were propagated from the errors in the flux ratios.

The physical conditions are presented in Table 3. As we already mentioned in §3.3, both blue-shifted components have very similar physical conditions and, therefore, the analysis

of their combination also returns similar conditions. The densities in the blue-shifted components amount to  $300 \text{ cm}^{-3}$ , while the red-shifted one has an  $n_e$  of about  $70 \text{ cm}^{-3}$ . These determinations are consistent with results found in previous spectroscopic studies that show densities ranging from 100 to  $600 \text{ cm}^{-3}$  in the nebula (e.g. Kwitter 1981; Mitra 1991; Esteban & Vilchez 1992; Fernández-Martín et al. 2012) and a density of  $< 100 \text{ cm}^{-3}$  in the ambient gas (Esteban & Vilchez 1992). The  $T_e$  derived from the [O III] line ratio is of about 9000 K in the blue-shifted components. This value is consistent with the analysis of Kwitter (1981) and Esteban & Vilchez (1992), who found  $T_e$  of about 8500-9500 K in different areas of the nebula from the [N II] and [O III] diagnostic ratios. The results of Mitra (1991) are the most discrepant, showing a  $T_e$  of about 16,000 K from the [O III] line ratio in a zone near our slit positions. Very recently, Fernández-Martín et al. (2012)

TABLE 2  
ATOMIC DATASET.

Ion	Transition Probabilities	Collisional Strengths
N <sup>+</sup>	Froese Fischer & Tachiev (2004)	Tayal (2011)
O <sup>+</sup>	Froese Fischer & Tachiev (2004)	Kisielius et al. (2009)
O <sup>2+</sup>	Froese Fischer & Tachiev (2004)	Palay et al. (2012)
Ne <sup>2+</sup>	Froese Fischer & Tachiev (2004)	Aggarwal & Keenan (1999)
S <sup>+</sup>	Podobedova et al. (2009)	McLaughlin & Bell (2000)
	Tayal & Zatsarinny (2010)	Tayal & Zatsarinny (2010)
Ar <sup>2+</sup>	Mendoza & Zeippen (1983)	Galavis et al. (1995)
Fe <sup>2+</sup>	Quinet (1996)	Zhang (1996)
	Johansson et al. (2000)	

have carried out the first study of NGC 6888 using integral field spectroscopy. Those authors do not obtain direct determinations of  $T_e([\text{O III}])$ , instead they estimate this quantity from direct determinations of  $T_e([\text{N II}])$  and assuming a relation between both electron temperatures based on photoionization models. In any case, three out of the nine apertures analyzed by Fernández-Martín et al. (2012) show  $T_e$  values of 8500-9000 K that are similar to our determinations, while the  $T_e$  is of about 6000-7000 K in the other six apertures.

The absence of the  $[\text{O III}] \lambda 4363$  line made impossible to obtain an empirical determination of the  $T_e$  for the redshifted component. So, we followed an alternative approach. If the  $+12 \text{ km s}^{-1}$  component is emitted by the ambient gas as previous studies have suggested (e.g. Chu 1988), the O/H ratio at the Galactocentric position of NGC 6888 would be given by the Galactic gradient of the O abundance (see §4.2). Then, the  $T_e$  of the ambient gas can be estimated fitting the O/H ratio predicted by the gradient with the O abundance derived from the observed  $[\text{O III}]$  and  $[\text{O II}]$  flux ratios of the blue range. The calculations return a  $T_e$  of  $7300 \pm 400 \text{ K}$ , giving us a temperature estimation for the ambient gas in the Cygnus OB1 association. The uncertainty comes from the error propagation of the abundance gradient and the assumed distances (see §4.2). This temperature is consistent with the predictions of the Galactic gradient of  $T_e([\text{O III}])$  derived by Deharveng et al. (2000) from the analysis of Galactic H II regions,  $7350 \pm 500 \text{ K}$ . The only previous estimation was done by Esteban & Vilchez (1992), who found a value of 6500 K applying empirical flux-flux calibrations.

#### 4.2. Abundances from the empirical method

Ionic abundances were computed from collisionally excited lines (CELs) using the PYNEB package and the atomic dataset of Table 2. The available ions in the blue spectra were O<sup>+</sup>, O<sup>2+</sup>, Ne<sup>2+</sup> and Fe<sup>2+</sup>, while O<sup>2+</sup>, N<sup>+</sup>, S<sup>+</sup> and Ar<sup>2+</sup> were available in the red spectra. The physical conditions,  $n_e$  and  $T_e$ , derived from the  $[\text{O II}]$  and  $[\text{O III}]$  diagnostic ratios in the blue spectra, respectively, were assumed for both spectral ranges. The final results are presented in Table 4. The errors were estimated as the quadratic sum of the independent contributions of  $n_e$ ,  $T_e$ , and flux ratio uncertainties.

Ionic abundances were also determined from recombination lines (RLs) for He<sup>+</sup> and C<sup>2+</sup>. The adopted values are also presented in Table 4. Currently, PYNEB provides optimal tools to calculate He<sup>+</sup> abundances. Several He I lines were detected in the spectra of each component and slit position. We used the effective recombination coefficients of Storey & Hummer (1995) for H I and those computed by Porter et al. (2012, 2013) for He I, whose calculations include corrections for collisional ex-

citation and self-absorption effects. The He<sup>+</sup>/H<sup>+</sup> ratios for each kinematical component correspond to the weighted average values of the ionic abundances obtained from some individual lines: He I  $\lambda\lambda 4388, 4713, 4922, 5016, 5876,$  and  $6678$  for the combined and  $-25 \text{ km s}^{-1}$  components; He I  $\lambda\lambda 4388, 4922, 5016,$  and  $5876$  for the  $-60 \text{ km s}^{-1}$  component; and He I  $\lambda\lambda 4922, 5016,$  and  $5876$  for the  $+12 \text{ km s}^{-1}$  component. The associated errors in Table 4 represent the quadratic sum of the weighted error and the standard deviation.

Our deep blue spectra allowed us to detect the faint C II  $\lambda 4267$  RL in the central kinematical component with a signal-to-noise ratio of 1.6 (see Fig. 3). After correcting for the reddening, we obtained a flux ratio  $I(\text{C II})/I(\text{H}\beta) = 0.0081 \pm 0.0051$  in the  $-25 \text{ km s}^{-1}$  component, which decreases to  $0.0069 \pm 0.0043$  for the combined component. PYNEB does not support abundance calculations from RLs of heavy-element ions yet, so we implemented our own routines with the effective recombination coefficients of Davey et al. (2000) to calculate the C<sup>2+</sup>/H<sup>+</sup> ratios. The errors were also determined as in the ionic abundances from CELs, though the flux uncertainty dominates the error in this case.

From the analysis of the blue-shifted components and their combination, total abundances of He, C, N, O, Ne, S, Ar, and Fe were calculated for NGC 6888. In §5, we present an extended discussion about the chemical composition of NGC 6888, while here we just focus on the calculations of the elemental abundances. The total O abundance was simply determined as the sum of O<sup>+</sup> and O<sup>2+</sup> in the blue range. Excluding O, the calculation of the total abundances of other elements required to correct for unseen ionization stages by means of ionization correction factors (ICFs). To calculate the total Fe abundances, the empirical fit of Rodríguez & Rubin (2005) was considered, accounting for the absence of Fe<sup>+</sup> and Fe<sup>3+</sup>. For He, C, N, Ne, S, and Ar, we considered the new set of ICFs recently developed by Delgado-Inglada et al. (2014, in press) and computed for a large grid of photoionization models. To estimate the ICFs and their errors, we used the same method as described by these authors in their work: we extract a subset from the PNe\_2014 models stored in the 3MdB database provided by the authors, selecting from them all the models with solar abundances and an effective temperature of about 50,000 K. The temperature value corresponds to the effective temperature of WR136 (Esteban et al. 1993; Crowther & Smith 1996). Then, the ICFs were computed in terms of the  $\text{O}^{2+}/(\text{O}^{+}+\text{O}^{2+})$  ratio and their values are presented in Table 5. The total abundances from ions only observed in the red range were calculated adopting the O<sup>+</sup>/H<sup>+</sup> and O<sup>2+</sup>/H<sup>+</sup> ratios from the blue range—therefore assuming the same O abundance in both slit positions. This approximation is reasonable since both zones have a similar O<sup>2+</sup>/H<sup>+</sup> ratio and probably similar ionization degrees. The total abundances are shown in Table 6, where we can note that the chemical abundances of the blue-shifted components are rather similar.

Table 6 also contains the elemental abundances of He, C, N, O, Ne, and Ar in the ambient gas of the Cygnus OB1 association as determined from the  $+12 \text{ km s}^{-1}$  component. S and Fe abundances were not derived due to emission lines associated with these elements were not detected in this component. These abundance calculations were possible taking into account that the O/H ratio is given by the Galactic O abundance gradient, which allowed us to derive the  $T_e([\text{O III}])$  in this kinematical component (see §4.1). The adopted gradient was:

$$12 + \log(O/H) = (8.869 \pm 0.049) - (0.045 \pm 0.005) \times R, \quad (2)$$

TABLE 3  
PHYSICAL CONDITIONS<sup>a</sup>.

Indicator		-60 km s <sup>-1</sup>	-25 km s <sup>-1</sup>	+12 km s <sup>-1</sup>	Combined
$n_e$ (cm <sup>-3</sup> )	[O II]	300:	310 ± 30	70:	310 ± 30
	[S II]	...	1250:	...	480:
$T_e$ (K)	[O III]	8790 ± 1140	9100 ± 810	7300 ± 400 <sup>b</sup>	9050 ± 810

<sup>a</sup> Colons indicate an error equal or higher than 50%.

<sup>b</sup> Fitting the O abundance to the Galactic O abundance gradient (see §4.1).

TABLE 4  
IONIC ABUNDANCES IN UNITS OF  $12+\log(X^{+i}/H^+)$ .

Ion	Range	-60 km s <sup>-1</sup>	-25 km s <sup>-1</sup>	+12 km s <sup>-1</sup>	Combined
He <sup>+</sup> <sup>a</sup>	Blue+Red	11.16 ± 0.09	11.23 ± 0.05	11.09 ± 0.12	11.21 ± 0.03
C <sup>2+</sup> <sup>a</sup>	Blue	...	8.88 ± 0.28	...	8.81 ± 0.28
N <sup>+</sup>	Red	7.74 ± 0.13	7.51 ± 0.08	7.67 ± 0.07	7.54 ± 0.08
O <sup>+</sup>	Blue	7.64 ± 0.23	7.41 ± 0.14	8.20 ± 0.12	7.45 ± 0.14
O <sup>2+</sup>	Blue	8.22 ± 0.17	8.09 ± 0.11	8.22 ± 0.12	8.11 ± 0.11
	Red	8.14 ± 0.17	8.01 ± 0.11	8.12 ± 0.08	8.02 ± 0.11
Ne <sup>2+</sup>	Blue	7.49 ± 0.27	7.39 ± 0.14	7.86 ± 0.18	7.40 ± 0.14
S <sup>+</sup>	Red	5.54 ± 0.25	5.44 ± 0.12	...	5.43 ± 0.09
Ar <sup>2+</sup>	Red	6.30 ± 0.17	6.38 ± 0.10	6.24 ± 0.11	6.36 ± 0.10
Fe <sup>2+</sup>	Blue	6.20 ± 0.63	5.85 ± 0.28	...	5.92 ± 0.30

<sup>a</sup> From RLs.

TABLE 5  
IONIZATION CORRECTION FACTORS.

Ratio	ICF <sup>a</sup>	-60 km s <sup>-1</sup>	-25 km s <sup>-1</sup>	+12 km s <sup>-1</sup>	Combined
He/H	He <sup>+</sup> +He <sup>2+</sup>	1.002 ± 0.003	1.001 ± 0.002	1.009 ± 0.004	1.001 ± 0.002
C/O	C <sup>2+</sup> /O <sup>2+</sup>	...	0.93 ± 0.01	...	0.92 ± 0.01
N/O <sup>b</sup>	N <sup>+</sup> /O <sup>+</sup>	1.68 ± 0.29	1.78 ± 0.33	1.34 ± 0.14	1.75 ± 0.33
Ne/O	Ne <sup>2+</sup> /O <sup>2+</sup>	1.05 ± 0.06	1.05 ± 0.05	1.00 ± 0.01	1.05 ± 0.05
S/O	S <sup>+</sup> /O <sup>+</sup>	3.90 ± 0.67	3.94 ± 0.63	...	3.94 ± 0.63
Ar/O	Ar <sup>2+</sup> /(O <sup>+</sup> +O <sup>2+</sup> )	1.11 ± 0.05	1.13 ± 0.07	1.07 ± 0.02	1.13 ± 0.06

<sup>a</sup> To be applied as: e.g. N/O = N<sup>+</sup>/O<sup>+</sup> × ICF(N<sup>+</sup>/O<sup>+</sup>).

<sup>b</sup> Assuming O<sup>+</sup>/H<sup>+</sup> and O<sup>++</sup>/H<sup>+</sup> from the blue range.

TABLE 6  
TOTAL ABUNDANCES IN UNITS OF  $12+\log(X/H)$ .

Element	-60 km s <sup>-1</sup>	-25 km s <sup>-1</sup>	+12 km s <sup>-1</sup>	Combined
He <sup>a</sup>	11.16 ± 0.09	11.23 ± 0.05	11.09 ± 0.12	11.21 ± 0.03
C <sup>a</sup>	...	8.93 ± 0.31	8.59 ± 0.10 <sup>b</sup>	8.86 ± 0.31
N	8.64 ± 0.31	8.52 ± 0.20	8.11 ± 0.16	8.54 ± 0.20
O	8.32 ± 0.14	8.17 ± 0.09	8.51 ± 0.07 <sup>b</sup>	8.20 ± 0.09
Ne	7.61 ± 0.35	7.49 ± 0.20	8.15 ± 0.21	7.51 ± 0.20
S	6.80 ± 0.38	6.81 ± 0.22	...	6.77 ± 0.20
Ar	6.34 ± 0.17	6.43 ± 0.11	6.27 ± 0.11	6.41 ± 0.11
Fe	6.59 ± 0.70	6.26 ± 0.34	...	6.33 ± 0.36

<sup>a</sup> From RLs.

<sup>b</sup> From the Galactic gradients of C and O (see §4.2 for details).

which comes from the linear fit of O abundances from CELs in H II regions (Esteban et al. 2005; García-Rojas & Esteban 2007) and is scaled to the Galactocentric distance of the Sun  $R_0 = 8.0 \pm 0.5$  kpc (Reid 1993). To compute the O/H ratio, we estimated that the Galactocentric distance of NGC 6888 is  $R = 7.8 \pm 0.5$  kpc, assuming a distance to NGC 6888 from the Sun of  $1.45 \pm 0.50$  kpc (Hipparcos parallax to the central star WR136; van Leeuwen 2007). Though the C II  $\lambda 4267$  RL was not detected in the red-shifted component, an estimate of its

C/H ratio is useful to compare with the C abundance found in the ring nebula. We estimated that quantity from the Galactic C gradient of Esteban et al. (2005) that is based on the analysis of the C II RL in H II regions. He, N, Ne, and Ar abundances were calculated using the same ICF scheme presented above. The values of these ICFs are also presented in Table 5.

We have compared the total abundances of C, N, and Ne calculated above with alternative abundance determinations that involve other ICF schemes. The ICFs of C were obtained from the photoionization models of Garnett et al. (1999), while N and Ne were derived using the ICFs proposed by Peimbert & Costero (1969). The Ne/H ratio was also calculated with the ICF of Pérez-Montero et al. (2007). In all cases, we found small differences within the estimated errors.

## 5. CHEMODYNAMICS OF NGC 6888

The presence of stellar ejecta in ring nebulae allows us to better understand the nucleosynthesis of massive stars and the effects of the H-burning reactions on the elements involved in the CNO cycle. A detailed analysis of the chemical composition and abundance ratios of these elements provides us valuable information, which in turns can help us to constrain the evolutive scenario of the massive stellar progenitor of the ring nebula. In the following sections, we will review the fi-

nal set of chemical abundances determined in this work for NGC 6888 and the surrounding medium as well as discuss their consequences on the CNO trace, and on the mass of the stellar progenitor when comparing with updated stellar evolution models.

### 5.1. Abundances and the CNO trace

In Table 7 we summarize the final set of gaseous abundances of He, C, N, O, Ne, S, Ar, and Fe in the ambient gas of the Cygnus OB1 association and in the ring nebula NGC 6888. For comparison, we also include in Table 7 the chemical composition of the solar vicinity represented by: the gaseous abundances of the Orion Nebula (Esteban et al. 2004; Rodríguez & Rubin 2005; Simón-Díaz & Stasińska 2011); abundances in nearby early B-type stars (Nieva & Przybilla 2012); and the solar ones considered in the stellar evolution models of Ekström et al. (2012), who adopted the solar abundances of Asplund et al. (2005), except for Ne which was taken from the analysis of nearby B-type stars of Cunha et al. (2006). In the second column of the table, we specified what kind of emission line was used in each abundance determination: CEL or RL. For clarification, we note that the information of this column only applies to the calculations of gaseous abundances and, thus, a direct comparison among the ambient gas, NGC 6888 and Orion is possible.

A comparison with the B-star abundances or the adopted solar ones is also possible, but after correcting the gaseous abundances of heavy-elements by their depletion onto dust grains. C, O, and Fe are the only elements of Table 7 where important depletions are expected. We have adopted the depletion values found in the solar neighborhood since NGC 6888 and the Cygnus OB1 association are only 1.45 kpc away from the Sun. In the Orion Nebula, the O depletion is estimated to be  $-0.12 \pm 0.03$  dex (Mesa-Delgado et al. 2009), while the Fe depletion amounts to  $-1.5 \pm 0.3$  dex (Nieva & Przybilla 2012). C is expected to be depleted in dust (PAH and graphite), though the study of its depletion is certainly problematic (see Mathis 1996). Following to Esteban et al. (1998), we have adopted a C depletion of  $-0.10$  dex. It should be noted that these depletion factors might be actually different due to the effects of possible dust destruction processes associated with the strong gas flows present in NGC 6888.

Table 7 also contains the elemental ratios of He, C, N, and Ne with respect to O for NGC 6888 and the ambient gas. The average ratios in the solar vicinity are also presented in Table 7 as determined as the mean of Orion, B stars, and the solar metallicity. The errors of these values represent the standard deviation. To carry out a consistent comparison of the observed ratios with the average ones of the solar vicinity, two aspects have been considered in their calculations. On the one hand, the C and O abundances of the nebular objects were corrected by their depletion onto dust grains as we previously mentioned. On the other hand, the elemental ratios should be calculated from gaseous abundances that were determined by the same method, i.e. using the same kind of emission lines (RLs or CELs); otherwise, ratios obtained through a combination of both emission lines can be severely affected by the so-called abundance discrepancy problem (see García-Rojas & Esteban 2007, and references therein). Although RLs emitted by O ions were not detected in our spectroscopic analysis, we managed to estimate the O/H ratio from RLs in the ambient gas and NGC 6888 to properly calculate their corresponding He/O and C/O ratios. These abundance values are included in Table 7. For the ambient gas, the O abundance from RLs was obtained

from the Galactic O gradient of Esteban et al. (2005) that is based on O II RLs. In the case of NGC 6888, the abundance discrepancy problem itself gave us a way of estimating the O/H ratio from RLs. From the analysis of the largest sample of Galactic H II regions, García-Rojas & Esteban (2007) found that on average the RL-CEL discrepancy amounts to  $0.16 \pm 0.06$  dex for  $O^+$  and  $0.25 \pm 0.02$  dex for  $O^{2+}$ . Then, the O/H ratio from RLs in NGC 6888 was estimated after adding the average discrepancies to the  $O^+$  and  $O^{2+}$  CEL-abundances derived through the empirical method. In Table 7, we can see that the RL-CEL discrepancy in the O abundance amounts to 0.23 dex for NGC 6888.

The comparison of the abundance ratios compiled in Table 7 indicates the striking abundance pattern found in NGC 6888. Within the errors, the gaseous abundances of the ambient gas are basically similar to the Orion ones. The elemental ratios shows small differences when comparing with the solar average ratios, but consistent within the errors. These discrepancies may be produced by biases induced by the line de-blending process and/or ionization degree discrepancies because the pointing mismatch of the blue and red spectral ranges. In general, the agreement between the ambient gas and the solar neighborhood is expected considering the small variation rates of the Galactic gradients and the proximity of NGC 6888.

The chemical composition and elemental ratios of NGC 6888 show a clear enrichment pattern. The Fe abundance is similar to that of the Orion Nebula, which is expected considering that massive stars do not enrich the ISM with Fe prior to the supernova phase. This fact also indicates that eventual dust destruction does not seem to affect the gas-phase Fe abundance in a substantial manner. S and Ar also present abundances consistent with Orion since these elements are not affected by the CNO burning chains. Attending to the He, N and O abundances, we can distinguish the trace of the CNO cycle: He and N overabundances, and an O deficiency, produced by complete cycles of the CN and ON chains through the reactions  $^{15}\text{N}(p, \alpha)^{12}\text{C}$  and  $^{17}\text{O}(p, \alpha)^{14}\text{N}$ , respectively. Previous studies of NGC 6888 have also found a similar enrichment trace and total abundances of He, N and O consistent with our determinations. For example, Esteban & Vilchez (1992) found He/H, N/H and O/H ratios of  $11.30 \pm 0.09$ ,  $8.40 \pm 0.35$  and  $8.11 \pm 0.28$  dex, respectively, from the analysis of a slit position near WR136. In a slit position near ours, Mitra (1991) also found similar abundances of about 11.30, 8.14 and 8.15 dex for He, N, and O, respectively. However, we should note that this slit position of Mitra (1991) is where we found the largest discrepancy of temperatures with respect to our results as we mentioned in §4.1. On the other hand, the Ne/O ratio seems to be consistent with the solar values within the uncertainties, while the Ne/H ratio is clearly below solar. Attending to the C/H and C/O ratios, the comparison with the solar neighborhood values reveals an anomalous pattern. In §5.4, we discuss in more detail these new findings in the framework of the CNO cycle and the nucleosynthesis of massive stars.

### 5.2. Chemical inhomogeneities in NGC 6888?

Up today, it is not completely clear that NGC 6888 is chemically inhomogeneous. A global analysis of the results from several slit positions distributed across the nebula (Kwitter 1981; Mitra 1991) and the integral field study of Fernández-Martín et al. (2012) shows that He, N, and O abundances vary from 10.95 to 11.35 dex, from 7.9 to 8.4 dex, and from 8.1 and 8.6 dex, respectively. However, it is necessary to emphasize that such a comprehensive comparison, mixing abundance de-



TABLE 7  
ABUNDANCE COMPARISON IN UNITS  $12+\log(X/H)$ .

Element	Method <sup>a</sup>	Ambient Gas	NGC 6888	Orion	Solar Neighborhood <sup>b</sup>	
					B stars	Solar
He	RL	11.09 ± 0.12	11.21 ± 0.03	10.991 ± 0.003	10.99 ± 0.01	10.93 ± 0.01
C	RL	8.59 ± 0.10 <sup>d</sup>	8.86 ± 0.31	8.37 ± 0.03	8.33 ± 0.04	8.39 ± 0.05
N	CEL	8.11 ± 0.16	8.54 ± 0.20	7.92 ± 0.09	7.79 ± 0.04	7.78 ± 0.06
O	CEL	8.51 ± 0.07	8.20 ± 0.09	8.52 ± 0.01	8.76 ± 0.05	8.66 ± 0.05
	RL	8.70 ± 0.12 <sup>e</sup>	8.43 ± 0.13 <sup>d</sup>	8.65 ± 0.03		
Ne	CEL	8.15 ± 0.21	7.51 ± 0.20	8.05 ± 0.03	8.09 ± 0.05	8.11 ± 0.04
S	CEL	...	6.77 ± 0.20	6.87 ± 0.06	...	...
Ar	CEL	6.27 ± 0.11	6.41 ± 0.11	6.39 ± 0.03	...	...
Fe	CEL	...	6.33 ± 0.36	6.00 ± 0.30	7.52 ± 0.03	7.45 ± 0.05
			Elemental Ratios <sup>e</sup>		Solar Average Ratios <sup>f</sup>	
He/O	RL	2.27 ± 0.17	2.66 ± 0.13		2.24 ± 0.03	
C/O	RL	-0.13 ± 0.16	0.41 ± 0.34		-0.33 ± 0.08	
N/O	CEL	-0.52 ± 0.18	0.22 ± 0.22		-0.84 ± 0.13	
Ne/O	CEL	-0.48 ± 0.22	-0.81 ± 0.22		-0.60 ± 0.06 / -0.65 ± 0.07 <sup>g</sup>	

<sup>a</sup> Only applies to the gaseous abundances calculated for the ambient gas, NGC 6888 and Orion.

<sup>b</sup> Chemical content in the Solar vicinity (see §5.1).

<sup>c</sup> From the Galactic gradients based on RLs (Esteban et al. 2005).

<sup>d</sup> Sum of the O<sup>+</sup> and O<sup>2+</sup> abundances from CELs after correcting them by the average RL-CEL discrepancy found in H II regions (see §5.1).

<sup>e</sup> Corrected by C and O depletion onto dust grains (see §5.1).

<sup>f</sup> Average ratios of Orion (after correcting for C and O depletions), B stars and solar. Errors account for the standard deviation.

<sup>g</sup> Computed adopting the Ne/H ratio for the Sun of  $7.93 \pm 0.10$  dex recommended by Asplund et al. (2009).

terminations of different authors and years, should be regarded with caution. The use of different atomic data or unreliable detections of the  $T_e$ -sensitive auroral lines are certainly important sources of error contributing to these variations. Comparing with Table 7, we see that the abundances we obtain are in the typical variation ranges.

Recently, Fernández-Martín et al. (2012) has suggested the existence of chemical inhomogeneities in NGC 6888 and that they can be produced by material ejected by the central star at different moments along the post-MS stages. In favor of this hypothesis, Humphreys (2010) points out that mass-loss episodes can happen through non-isotropic and powerful ejections, which can explain the chemical inhomogeneities across a ring nebula associated with a massive star. This hypothesis is also plausible according to the nucleosynthesis predicted by stellar evolution models of massive stars. Figs. 4 and 5 show the time variation of different abundance ratios in the material ejected by 25 and 40  $M_{\odot}$  stars (see §5.3 for more details). If these temporal abundance variations are actually transformed into spatial abundance variations across NGC 6888, our assumption of considering the same O/H ratio in our two slit positions to derive the N abundance (see §4.2) might be inappropriate. However, taking into account that: (a) our positions are very close each other (less than 10'' apart, see Fig. 1), and (b) the abundances obtained by Mitra (1991) in a nearby position are consistent with our determinations, it seems reasonable to consider that NGC 6888 is chemically homogeneous at least in the area covered by our slit positions.

### 5.3. Comparison with stellar evolution models

The central star of NGC 6888, WR136, has a present-day mass of about 15  $M_{\odot}$  (Hamann et al. 2006), and has just entered the WR phase according to its classification as an early nitrogen-type WR star (WN6(h); van der Hucht 2001). The detection of X-ray emission in NGC 6888 is an observational clue that support this idea (e.g. Wrigge et al. 1994), indicating that the WR wind is interacting with the previous RSG shell. Addi-

tionally, it has been estimated that NGC 6888 has a dynamical age of about ~20,000-40,000 years (see §1). This ring nebula is thus a relatively recent event in the evolution of WR136. Surely, the chemical evolution of the NGC 6888+WR136 system in the light of this single-star scenario could suffer important modifications if the presence of a binary companion is confirmed as previous works have suggested (see Stevens & Howarth 1999, and references therein). Since the binarity of WR136 is still an unresolved issue, hereinafter we will focus on the single-star case.

Under the above considerations, we aim to constrain the mass of the progenitor of the WR136 star combining the updated stellar evolution models of Ekström et al. (2012) and Georgy et al. (2012) with the new set of gaseous abundances of He, C, N, O, and Ne determined in this paper. Esteban & Vilchez (1992) were the first to attempt this question in NGC 6888 from their spectroscopical analysis in the optical range. Comparing the gaseous abundances of He, N, and O with the enrichment pattern predicted by the stellar evolution models of Maeder (1990), those authors concluded that NGC 6888 and WR136 were originated from a stellar progenitor with a mass between 25 and 40  $M_{\odot}$ . Since the early study of Esteban & Vilchez (1992), stellar evolutive models have been improved in several aspects, incorporating the effects of stellar rotation, new recipes to account for the mass-loss rates, or updating nuclear reaction rates (see Ekström et al. 2012, and references therein). Recently, Toalá & Arthur (2011) have attempted a similar approach using updated stellar evolution models and the N/O ratio derived by Esteban & Vilchez (1992). However, these authors only focused on discussing the effects of stellar rotation on the observed abundance pattern and confirmed that the observed trace is consistent with the fact that WR136 is an early nitrogen-type WR star.

In our analysis we have considered evolution models for stars with masses of 25, 32, 40 and 60  $M_{\odot}$ . To carry out the calculations, we have assumed that the stellar surface abundances given by the models are representative of the chemical

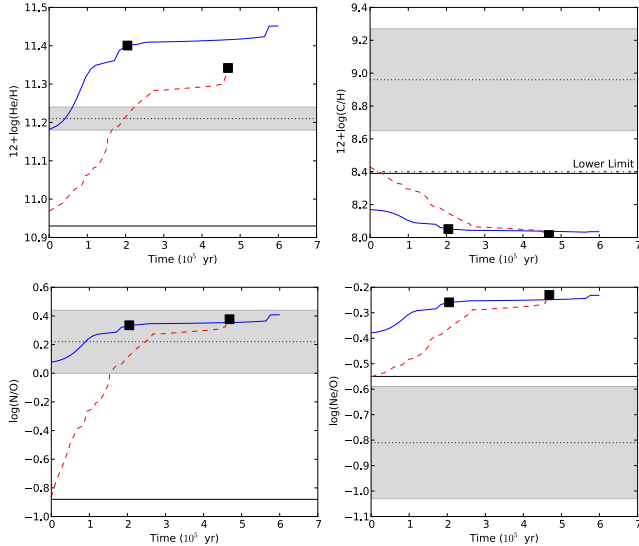


FIG. 4.— He/H, C/H, N/O, and Ne/O abundance ratios of the stellar material ejected by a  $25 M_{\odot}$  star from the stellar evolution models of Ekström et al. (2012) and Georgy et al. (2012) with rotation (blue solid line) and without rotation (red dashed line). The origin in abscissa corresponds to the onset of enhanced mass loss at the beginning of the RSG phase. The onset of the WR phase is indicated by the black square in both rotational and non-rotational stellar models. The horizontal solid lines correspond to the solar values as adopted by the stellar evolution models (see §5.1 for details). The grey bands represent the observed abundances and their uncertainties. The dotted-dashed line almost overlapped with the solar one is the lower limit in the C/H ratio, which was estimated from the minimum value of C abundance compatible with the observational data (see §5.3 for details).

composition of the stellar wind. The surface abundances of H, He, C, N, O, and Ne given by the models were weighted by the mass-loss rate and then integrated over time using the composite trapezoidal rule. The initial integration point was set in all models at the moment in which the massive star reaches the minimum effective temperature,  $T_{eff}$ , after finishing the MS stage. This point exactly coincides with the onset of enhanced mass loss at the beginning of the RSG phase (or LBV phase for the most massive stars) and, therefore, our approximation does not include material expelled during the MS stage. As Toalá & Arthur (2011) argued, the contribution of the material ejected during the MS can be ignored due to it is spread throughout a much more extended bubble with a size of several tens of parsecs, while the RSG and WR wind material would form a ring nebula in the immediate surroundings around the central star. This last picture is consistent with the current view of the NGC 6888+WR136 system described in the first paragraph of this section. To properly compare the model predictions with the observed abundances, the integration results for He, C, N, O, and Ne relative to H and/or O were converted from fractional mass to number units through the atomic weight of the elements. For illustration, we present in Figs. 4 and 5 the He/H, C/H, N/O, and Ne/O ratios for the stellar material ejected along time by a 25 and  $40 M_{\odot}$  star, respectively. We used the He/H and C/H ratios to explore the variation of the He and C abundances because these ratios are calculated from the intensity of RLs in both numerator and denominator. N and Ne abundances are determined from CELs and therefore we have used their ratios with respect to O abundances, which are also obtained from CELs. Using those particular abundance ratios, we avoid abundance discrepancy effects in the comparison.

A quick look of Figs. 4 and 5 shows us the main differences between the rotational (dashed line) and non-rotational

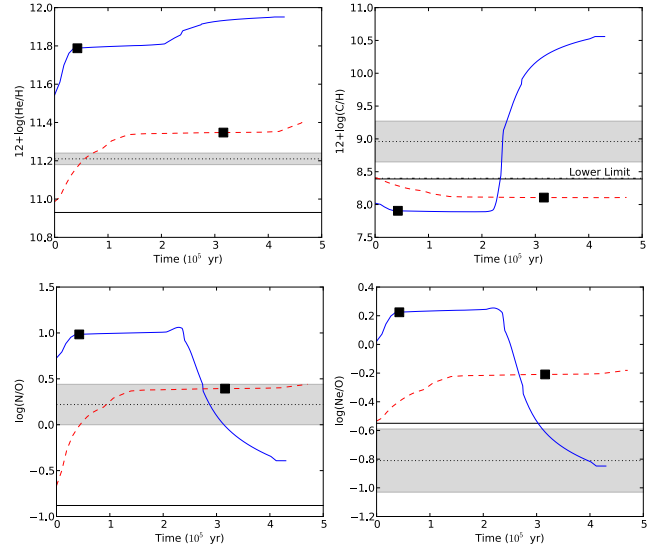


FIG. 5.— Same as Fig. 4 for a  $40 M_{\odot}$  star.

(solid line) models. It must be noted that rotational models are calculated assuming a very large initial rotation velocity of about  $300 \text{ km s}^{-1}$ , much larger than the present-day value of  $37 \text{ km s}^{-1}$  calculated by Gräfener et al. (2012) for WR136. One of the most important effects of the stellar rotation is that the WR phase starts much earlier than what is predicted by the non-rotational models. Rotational models even predict that in the case of the  $60 M_{\odot}$  star the WR phase can be initiated during the MS stage. An interesting note about the new evolution models is also that the minimum mass for starting the WR phase is lower than in previous models, being now 20 and  $25 M_{\odot}$  for the rotational and non-rotational cases, respectively. In Figs. 4 and 5 the onset of the WR phase is indicated by squares. In all cases, this was set following the definitions of stellar types of Eldridge et al. (2008) and the considerations discussed by Georgy et al. (2012). The localization of this point is the first constraint that allows us to distinguish what evolution models are consistent with the current picture of the NGC 6888+WR136 system. According to the lifetimes of the WR phase estimated by Georgy et al. (2012), only the rotational models of 25 and  $32 M_{\odot}$ , and the rotational and non-rotational models of 40 and  $60 M_{\odot}$  are consistent with the dynamical age estimated for NGC 6888.

In Figs. 4 and 5, we can also see that the abundance patterns produced by both rotational and non-rotational models are very different. Qualitatively, the results for stellar models of 25, 32, and  $40 M_{\odot}$  are in general rather similar, though the timeline is certainly different. The C/H ratio presents the most distinctive pattern. Non-rotational models start the RSG phase with a C/H ratio similar to the solar value and rotational ones somewhat lower than solar. The C/H remains almost constant but, at a given moment, the enrichment pattern of the  $25 M_{\odot}$  stellar model behaves in a different way than those of the 32 and  $40 M_{\odot}$ . In both, the rotational and non-rotational cases of the  $25 M_{\odot}$  star, the C/H continues moderately decreasing until it reaches a saturation value that remains almost constant over time. The 32 and  $40 M_{\odot}$  stellar models show that: while non-rotational models keep a rather constant C/H ratio along time, rotational ones exhibit a remarkably strong C enrichment. This C is produced by  $3\alpha$  reactions in the stellar interior, and transported to the stellar surface through efficient dredge-up and mixing processes as well as deep convective layers boosted

by the stellar rotation. The abundance ratios of He/H, N/O, and Ne/O show a qualitatively similar behavior. Rotational models predict an important initial increase of He/H, N/O, and Ne/O at the beginning of the RSG phase, once again related to the effects of stellar rotation. Instead, non-rotational models clearly start the RSG phase ejecting material with solar abundance ratios. The case of the  $60 M_{\odot}$  stellar model produces abundance patterns with enhanced elemental ratios and slightly different behaviors than the models for stars of lower masses. However, we have not discussed it because this model is discarded as we will comment below.

We have compared the observed abundance ratios of NGC 6888 with the different model results. Given the current picture of the NGC 6888+WR136 system, the different ratios are associated with material that was probably ejected about one dynamical age of NGC 6888 ago or before the beginning of the WR phase. The observed ratios and their observational uncertainties are represented in Figs. 4 and 5 by means of grey bands over the predictions of the stellar evolution models. The C/H and Ne/O ratios present puzzling patterns that do not fit the model predictions as we discuss in §5.4 and, therefore, our analysis is restricted to the He/H and N/O ratios. Attending to the time constraint of the dynamical age of the nebula and the He/H and N/O ratios, we found that our observations can be reproduced by the rotational model for a  $25 M_{\odot}$  star, and by the non-rotational models for 40 and  $60 M_{\odot}$  stars. The model of  $60 M_{\odot}$  can be rejected due to the inclusion of rotation in the new stellar evolution models predicts that the WR phase is initiated during the MS stage, which is not compatible with our current knowledge of WR136. Since rotation is certainly a property of every star in the Universe, our analysis suggests that NGC 6888 and WR136 are probably the evolutive products of a stellar progenitor with a mass lower than  $40 M_{\odot}$ .

The comparison with stellar evolution models can also give an estimation of the time scale when the processed material was ejected by WR136. The non-rotational model of  $60 M_{\odot}$  predicts that the He/H and N/O ratios are representative of material ejected in different time scales before the onset of the WR phase. Considering the error bars, we obtained that the He/H ratio would represent material ejected about 15,000 years ago, while the material with the observed N/O ratio was expelled about 130,000 years ago. Instead, the rotational model of  $25 M_{\odot}$  and the non-rotational model of  $40 M_{\odot}$  produce more consistent results, where both observed ratios represents material ejected about 160,000 years and 260,000 years, respectively. If the observed material was ejected during the RSG phase and assuming that the RSG shell expanded with velocities similar to the RSG wind ( $10 - 20 \text{ km s}^{-1}$ ; van Marle et al. 2005), we can estimate that the RSG shell has spent about 120,000 – 240,000 years to reach the location of our slit positions, about 2.5 pc away from the central star. This estimation is more consistent with the results found for 25 and  $40 M_{\odot}$  stars.

#### 5.4. The puzzling C and Ne abundance patterns

Unlike He and N, the comparison of the C abundance in NGC 6888 with the solar vicinity reveals at first look an enrichment pattern that does not fit the expectations of the CNO cycle (see Table 6 and §5.1) and neither the C/H ratio can be reproduced by any stellar evolution model. In the case of the Ne abundance, we can see in Figs. 4 and 5 that the Ne/O ratio is always below the model predictions even considering the uncertainties.

In the H-burning through the CNO cycle, C and O act as

simple catalyzers driving the fusion reactions that convert  $^1\text{H}$  into  $^4\text{He}$  along the MS. However, given the different rates of the component reactions, the CNO cycle modifies the initial composition of the stellar material. The cycle efficiency is dominated by the slowest reaction,  $^{14}\text{N}(p, \gamma)^{15}\text{O}$ , responsible for the accumulation of N synthesized at the expense of C and O. We would then expect that the C/H ratio in NGC 6888 should be lower than the gaseous C abundance at the Galactic position of the nebula. At the Galactocentric position of the nebula, the C/H ratio of the ambient gas should range between 8.4 and 8.6 dex, which are given by Orion and the Galactic C gradient, respectively. In contrast, we have estimated that the gaseous C abundance is about  $8.9 \pm 0.3$  dex. We have estimated the strictest lower limit for the C/H ratio permitted by our data assuming that the continuum at the base of the C II line is at the higher level of the noise estimated around the line. Following this procedure we obtain  $I(\text{C II } \lambda 4267)/I(\text{H}\beta) = 0.0018$ , which gives an abundance of  $12+\log(\text{C}/\text{H}) \simeq 8.3$ . Assuming this value, the C/H ratio of NGC 6888 becomes similar to the expected one for its galactocentric position, but only considering non-rotational models for the 25, 32, and  $40 M_{\odot}$  at the beginning of the RSG phase. However, as we have already argued, rotation is an inherent property of every star and, therefore, this may be a rather improbable case. Indeed, rotational models predict C/H ratios lower than the estimated lower limit (see Figs. 4 and 5).

If the C, N and O measured in NGC 6888 are produced by the CNO cycle, the sum of their abundances by mass should be similar to that of the ambient gas or, for example, the Orion Nebula. Calculating these numbers we find that using the nominal value of the  $12+\log(\text{C}/\text{H})$  of 8.9 dex, the sum of the CNO nuclei in NGC 6888 is a factor of two larger than expected and therefore an additional source of C should be necessary. This would imply that part of the freshly made C from the  $3\alpha$  reactions was dredge-up to the stellar surface at the moment of the ejection of the bulk of the nebular material. On the other hand, assuming the strict lower limit of  $12+\log(\text{C}/\text{H}) \sim 8.3$  estimated above, the sum of CNO particles is in broad agreement with that expected by the CNO cycle, but implying that most of the N comes from the destruction of O, which is not a completely satisfactory solution.

Rola & Pelat (1994) argued that flux measurements of emission lines with low signal-to-noise ratio can be systematically overestimated, and such effect increases as the signal-to-noise ratio decreases. This effect may be affecting our C abundances, although some authors have advocated against it (see Mathis & Liu 1999; Esteban 2002). Following the formulation of Rola & Pelat (1994) provided to estimate such effect, we found that the measured flux of the C II RL is reduced by around half. From the new flux ratio, we estimated a total C abundance of  $8.6 \pm 0.3$  dex. This value is certainly consistent with the gaseous C abundance of the ambient gas, but it still has the same issues than our lower limit (see previous paragraphs).

It is interesting to compare the C abundance determined here with the only previous estimation available in the literature for NGC 6888 obtained by Moore et al. (2006). Under geometrical assumptions and considering that most of the carbon is double-ionized, those authors estimated a C/H ratio of  $7.6 \pm 0.3$  dex from the analysis of the UV absorption line C III  $\lambda 911$  along the line of sight to the central star WR136. Correcting by C depletion onto dust grains, only the higher limit of this estimation is consistent with the results of the rotational stellar evolution models for all stellar masses. Obviously, there is a

large discrepancy between the C/H ratio determined by Moore et al. (2006) and us. This puzzling situation points out the real need of deriving more accurate C abundances in NGC 6888.

Finally, as we already said in §5.1, the Ne/O ratio of NGC 6888 seems to be solar within the uncertainties. However, in Figs. 4 and 5 it is clear that the Ne/O ratio is below the model predictions. In Table 7 we can also see that the Ne/H ratio in the ambient gas and the solar vicinity are rather consistent, while NGC 6888 has a lower Ne abundance even within the uncertainties. The gaseous abundance of Ne in the Orion Nebula is indeed a reliable reference to compare with. From photoionization models with the data observed by Esteban et al. (2004), Simón-Díaz & Stasińska (2011) derived a Ne/H ratio in Orion of 8.05 dex (quoted in Table 7), while Rubin et al. (2011) obtained a total Ne abundance of  $8.00 \pm 0.03$  dex from measurements of the infrared [Ne II] and [Ne III] CELs without requiring any ionization correction factor. Comparing with these values, the Ne/H in NGC 6888 is of about 0.5 dex lower. To understand such behavior we should invoke the action of the NeNa cycle (e.g. Arnould & Mowlavi 1993) in a higher intensity than the models assume. This cycle destroys Ne nuclei in the hydrogen burning zone at temperatures of about  $3.5 \times 10^7$ , values that can be reached in massive star cores. In fact, the action of NeNa cycle can be the reason of the large Na abundances found in yellow supergiants. Denissenkov (2005) has proposed that rotational mixing of Na between the convective core and the radiative envelope in the MS progenitors of the more massive yellow supergiants can account for the Na enhancements observed. This would be a possible solution for the puzzling Ne underabundance observed in NGC 6888.

#### 6. CARBON CONTENT IN RING NEBULAE: A CHALLENGE FOR 10M TELESCOPES AND SPACE OBSERVATORIES

Until now, the chemical content of C in ring nebulae has been unknown and, therefore, we completely lacked on one of the fundamental parameters that constrains the enrichment trace of the CNO cycle. This has hindered for years a comprehensive comparison of the observed CNO trace with the predictions of nucleosynthesis models of massive stars. The determination of C abundances from the analysis of emission line spectra is in general a challenging task. In the particular case of ring nebulae, given their inherent low surface brightness ( $F(H\beta) \leq 10^{-15}$  erg s $^{-1}$  cm $^{-2}$  arcsec $^{-2}$ ), it is certainly a challenge to overcome that needs the use of state-of-the-art technology in the largest aperture ground-based telescopes and space-borne observatories.

Recently, Stock et al. (2011) have attempted without success the detection of [C I] lines at 8727, 9824, and 9850 Å in a sample of southern ring nebulae making use of the 3.6 m ESO New Technology Telescope and the 8 m Very Large Telescope. As the authors argued, these emission lines are usually observed in certain astrophysical contexts such as H II regions or planetary nebulae. However, they may not be used as reliable empirical diagnostics since their emissions mainly arise behind the ionization front in a radiation-bounded region, produced by radiative transitions of neutral carbon previously excited by collision with free electrons.

The detection of the brightest emission lines of carbon requires observations from space. On the one hand, the far-IR range contains the [C II] 158  $\mu$ m fine-structure line. Unfortunately, the use of this line is problematic because its emission predominantly comes from photodissociation regions (e.g. Lebouteiller et al. 2012). This issue is also coupled with other

problems related to IR spectroscopy such as ICFs, collisional de-excitation effects at modest electron densities, or still large sizes of the IR spectrograph beams (see Garnett et al. 2004). The *Herschel* key problem MESS (Mass-loss of Evolved StarS; Groenewegen et al. 2011) is the only project that today can provide crucial information about the C abundance in ring nebulae making use of the [C II] 158  $\mu$ m, but no results have come out in this sense yet. On the other hand, the UV range presents the well-known prominent carbon features C II]  $\lambda$ 2326 and C III]  $\lambda$ 1907+09, which are only observable by the *Hubble Space Telescope* (*HST*). Unfortunately, the *HST* have only accepted a single proposal (program ID: 8568) since its launch to investigate the C content in NGC 6888 using the Space Telescope Imaging Spectrograph and no C features were observed then. Since 2009 the unprecedented high-sensitivity of the Cosmic Origin Spectrograph at the *HST* represents the only opportunity to detect the UV carbon lines, though we have still to take into account that UV observations can be severely affected by the uncertainties in the reddening correction and the strong dependence of the emissivity of UV CELs on the adopted electron temperature. Additionally, the C II]  $\lambda$ 2326 line is affected by similar concerns to those of the [C I] and [C II] 158  $\mu$ m lines: given the low ionization potential of neutral carbon (11.2 eV), it is expected the presence of C $^+$  behind the ionization front in a radiation-bounded region.

Thanks to new generations of CCDs with improved efficiency in the blue and the use of large aperture telescopes, determinations of the C/H ratio have become feasible with the detection of the C II  $\lambda$ 4267 RL. Based on this RL, for example, it has been possible the study of radial gradients of C in the Galaxy and in a few external spiral galaxies (e.g. Esteban et al. 2009, 2013). This emission line is however very faint, with a flux of about  $0.001 - 0.01 \times F(H\beta)$ , requiring very deep observations for its detection. Up today, the C II RL has only been detected in the Galactic ring nebulae NGC 6888 (this work) and NGC 7635 (Rodríguez 1999; Moore et al. 2002; Mesa-Delgado & Esteban 2010). In the particular case of NGC 7635, Mesa-Delgado & Esteban (2010) obtain  $12 + \log(C/H)$  values between 8.6 and 9.0 in several areas of the nebula, abundances much larger than those expected from the Galactic abundance gradient, that should be about 8.45. As we can see, the behavior of C/H ratios in these two objects is rather similar and completely different to that shown by whatever H II region.

Mesa-Delgado & Esteban (2010) discussed the possible reasons of the high C/H ratios found in NGC 7635, and most of their arguments can be also applied for NGC 6888. Firstly, NGC 7635 is very unlikely that has suffered a pollution of C processed by the ionizing central star. It is an interstellar bubble blown by the young, massive central MS star BD+60° 2522 of spectral type O6.5 IIIef (e.g. Dawanas et al. 2007). A mass of 45  $M_{\odot}$  has been estimated for BD+60° 2522 (Howarth & Prinja 1989; Dawanas et al. 2007), but it is thought that the star evolved from a progenitor of 60  $M_{\odot}$  (Dawanas et al. 2007). Christopoulou et al. (1995) concluded that NGC 7635 nebula has a dynamical age of about 50,000 years. In contrast, NGC 6888 has been ejected by a post-MS star. In both cases, stellar evolution models do not predict a C enhancement in the evolution phase of the central stars when the nebular material was ejected. From the theoretical point of view, the only way to understand the strong C enrichment in the outer layers of the stellar progenitor of NGC 6888 –as discussed in §5.3, is that the rotational-induced dredge-up of processed C takes place earlier in the evolution of the star, before the star enters the WR phase. Another possible explanation of a local increase

of C may be due to the destruction of carbon-rich dust by the shocks associated with the expanding windblown bubble. This was already suggested by Moore et al. (2002) for NGC 7635. Esteban et al. (1998) estimated that the destruction of all the carbon locked-up onto dust grains in the Orion Nebula would increase the measured gas-phase C/H ratio by only about 0.1 dex. An increase of such magnitude cannot explain completely the large C overabundances measured in the two ring nebulae with respect to the C/H ratios expected by the abundance gradients. A third explanation can be related to an abnormal enhancement in the intensity of the C II  $\lambda 4267$  RL. However, Escalante et al. (2012) have recently concluded that C II  $\lambda 4267$  is not affected by any kind of fluorescence effect and therefore any possible mechanism that could affect the intensity of this line is actually unknown.

## 7. CONCLUSIONS

We present results based on echelle spectroscopy of the Galactic ring nebula NGC 6888 taken with the High Dispersion Spectrograph at the 8.2 m Subaru Telescope. The nebula is associated to the central star WR136, a massive Wolf-Rayet (WR) star of the WN6(h) sequence. The spectra are very deep and cover the optical range from 3700 to 7400 Å. The high-spectral resolution of  $R \sim 12,000$  permits to distinguish three kinematical components at  $-60$ ,  $-25$ , and  $+12$  km $^{-1}$ . The two blue-shifted components correspond to gaseous filaments or clumps in the approaching side of the nebula, and the red-shifted one to the ambient gas that surrounds the Cygnus OB1 association. We have derived the physical conditions,  $n_e$  and  $T_e$ , for each kinematical component. We obtain direct determinations of  $T_e$ ([O III]) for the two blue-shifted components who belong to the shell of NGC 6888 itself, and an indirect estimation for the ambient gas. We determine ionic and total abundances of several elements from collisionally excited lines (CELs) as well as those of He and C from recombination lines (RLs). A comprehensive comparison of the gaseous abun-

dances shows us that the effects of the CNO nucleosynthesis are well identified in He, N, and O, while elements such as Ar, S, and Fe –which are not involved in the cycle– present abundances consistent with the solar values and the ambient gas. This is the first time that the C II  $\lambda 4267$  RL is detected in a ring nebula associated with a WR star, allowing to investigate the trace of the CNO cycle in a massive star ejecta. Although the detection of the C II line has a low signal-to-noise ratio, the C abundance seems to be higher than the predictions of recent stellar evolution models of massive stars, even including the effects of stellar rotation. Further investigations are needed making use of large aperture telescopes to obtain more reliable measurements for this faint emission line. The Ne abundance also presents a puzzling pattern, being lower than the model predictions and lower than the solar vicinity. These Ne deficiency may be also related to the Na overabundances observed in yellow supergiants. The action of the NeNa cycle occurring in a higher rate than the models assume may explain these results. Attending to the constraints imposed by the dynamical timescale of the nebula and the observed He/H and N/O ratios, the comparison with the predictions of stellar evolution models indicates that the initial mass of the stellar progenitor of NGC 6888 should be between 25 and 40  $M_{\odot}$ .

We are grateful to the referee, D. Stock, for his careful reading and proposed suggestions, which have help us to constrain the reliability of the carbon abundances. We thank to T. H. Puzia, J. Arthur, G. Meynet and, especially, M. Cerviño for their help with the evolutionary tracks. AMD thanks to R. Lachaume for being his PYTHON guru. AMD acknowledges support from Comité Mixto ESO-Chile, a Basal-CATA (PFB-06/2007) grant and the FONDECYT project 3140383. JGR and CEL acknowledge support from the Spanish Ministerio de Economía y Competitividad (project AYA2011-22614).

*Facilities:* SUBARU (HDS).

## REFERENCES

- Aggarwal, K. M. & Keenan, F. P. 1999, *ApJS*, 123, 311  
 Arnould, M. & Mowlavi, N. 1993, in *Astronomical Society of the Pacific Conference Series*, Vol. 40, IAU Colloq. 137: Inside the Stars, ed. W. W. Weiss & A. Baglin, 310–323  
 Arthur, S. J. 2007, in *Revista Mexicana de Astronomía y Astrofísica*, vol. 27, Vol. 30, *Revista Mexicana de Astronomía y Astrofísica Conference Series*, 64–71  
 Asplund, M., Grevesse, N., & Sauval, A. J. 2005, in *Astronomical Society of the Pacific Conference Series*, Vol. 336, *Cosmic Abundances as Records of Stellar Evolution and Nucleosynthesis*, ed. T. G. Barnes, III & F. N. Bash, 25  
 Asplund, M., Grevesse, N., Sauval, A. J., & Scott, P. 2009, *ARA&A*, 47, 481  
 Bohkarev, N. G. 1988, *Nature*, 332, 518  
 Cappa, C., Niemela, V. S., Martín, M. C., & McClure-Griffiths, N. M. 2005, *A&A*, 436, 155  
 Cardelli, J. A., Clayton, G. C., & Mathis, J. S. 1989, *ApJ*, 345, 245  
 Christopoulou, P. E., Goudis, C. D., Meaburn, J., Dyson, J. E., & Clayton, C. A. 1995, *A&A*, 295, 509  
 Chu, Y.-H. 1981, *ApJ*, 249, 195  
 —, 1988, *PASP*, 100, 986  
 Crowther, P. A. & Smith, L. J. 1996, *A&A*, 305, 541  
 Cunha, K., Hubeny, I., & Lanz, T. 2006, *ApJ*, 647, L143  
 Davey, A. R., Storey, P. J., & Kisielius, R. 2000, *A&AS*, 142, 85  
 Dawanas, D. N., Wardana, A., & Malasan, H. L. 2007, *Ap&SS*, 312, 23  
 Deharveng, L., Peña, M., Caplan, J., & Costero, R. 2000, *MNRAS*, 311, 329  
 Delgado-Inglada, G., Morisset, C., & Stasińska, G. 2014, *MNRAS*, in press  
 Denissenkov, P. A. 2005, *ApJ*, 622, 1058  
 Dopita, M. A., Bell, J. F., Chu, Y.-H., & Lozinskaya, T. A. 1994, *ApJS*, 93, 455  
 Ekström, S., Georgy, C., Eggenberger, P., Meynet, G., Mowlavi, N., Wyttenbach, A., Granada, A., Decressin, T., Hirschi, R., Frischknecht, U., Charbonnel, C., & Maeder, A. 2012, *A&A*, 537, A146  
 Eldridge, J. J., Izzard, R. G., & Tout, C. A. 2008, *MNRAS*, 384, 1109  
 Escalante, V., Morisset, C., & Georgiev, L. 2012, *ArXiv e-prints*  
 Esteban, C., 2002, in Henney W. J., Franco J., Martos M., eds., *Revista Mexicana de Astronomía y Astrofísica Conference Series*, 12, p. 56  
 Esteban, C., Bresolin, F., Peimbert, M., García-Rojas, J., Peimbert, A., & Mesa-Delgado, A. 2009, *ApJ*, 700, 654  
 Esteban, C., Carigi, L., Copetti, M. V. F., García-Rojas, J., Mesa-Delgado, A., Castañeda, H. O., & Péquignot, D. 2013, *MNRAS*, 433, 382  
 Esteban, C., García-Rojas, J., Peimbert, M., Peimbert, A., Ruiz, M. T., Rodríguez, M., & Carigi, L. 2005, *ApJ*, 618, L95  
 Esteban, C., Peimbert, M., García-Rojas, J., Ruiz, M. T., Peimbert, A., & Rodríguez, M. 2004, *MNRAS*, 355, 229  
 Esteban, C., Peimbert, M., Torres-Peimbert, S., & Escalante, V. 1998, *MNRAS*, 295, 401  
 Esteban, C., Smith, L. J., Vilchez, J. M., & Clegg, R. E. S. 1993, *A&A*, 272, 299  
 Esteban, C. & Vilchez, J. M. 1992, *ApJ*, 390, 536  
 Esteban, C., Vilchez, J. M., Smith, L. J., & Clegg, R. E. S. 1992, *A&A*, 259, 629  
 Esteban, C., Vilchez, J. M., Manchado, A., & Edmunds, M. G. 1990, *A&A*, 227, 515  
 Fernández-Martín, A., Martín-Gordón, D., Vilchez, J. M., Pérez Montero, E., Riera, A., & Sánchez, S. F. 2012, *A&A*, 541, A119  
 Freyer, T., Hensler, G., & Yorke, H. W. 2003, *ApJ*, 594, 888  
 —, 2006, *ApJ*, 638, 262  
 Froese Fischer, C. & Tachiev, G. 2004, *Atomic Data and Nuclear Data Tables*, 87, 1

- Galavis, M. E., Mendoza, C., & Zeppen, C. J. 1995, *A&AS*, 111, 347
- García-Rojas, J. & Esteban, C. 2007, *ApJ*, 670, 457
- García-Segura, G., Langer, N., & Mac Low, M.-M. 1996a, *A&A*, 316, 133
- García-Segura, G., Mac Low, M.-M., & Langer, N. 1996b, *A&A*, 305, 229
- Garnett, D. R., Kennicutt, R. C., & Bresolin, F. 2004, *ApJ*, 607, L21
- Garnett, D. R., Shields, G. A., Peimbert, M., Torres-Peimbert, S., Skillman, E. D., Dufour, R. J., Terlevich, E., & Terlevich, R. J. 1999, *ApJ*, 513, 168
- Georgy, C., Ekström, S., Meynet, G., Massey, P., Levesque, E. M., Hirschi, R., Eggenberger, P., & Maeder, A. 2012, *A&A*, 542, A29
- Gräfener, G., Vink, J. S., Harries, T. J., & Langer, N. 2012, *A&A*, 547, A83
- Groenewegen, M. A. T., Waelkens, C., Barlow, M. J., Kerschbaum, F., García-Lario, P., Cernicharo, J., Blommaert, J. A. D. L., Bouwman, J., Cohen, M., Cox, N., Decin, L., Exter, K., Gear, W. K., Gomez, H. L., Hargrave, P. C., Henning, T., Hutsemékers, D., Ivison, R. J., Jorissen, A., Krause, O., Ladjal, D., Leeks, S. J., Lim, T. L., Matsuura, M., Nazé, Y., Olofsson, G., Ottensamer, R., Polehampton, E., Posch, T., Rauw, G., Royer, P., Sibthorpe, B., Swinyard, B. M., Ueta, T., Vamvatira-Nakou, C., Vandenbussche, B., van de Steene, G. C., van Eck, S., van Hoof, P. A. M., van Winckel, H., Verdugo, E., & Wesson, R. 2011, *A&A*, 526, A162
- Gruendl, R. A., Chu, Y.-H., Dunne, B. C., & Points, S. D. 2000, *AJ*, 120, 2670
- Hamann, W.-R., Gräfener, G., & Liermann, A. 2006, *A&A*, 457, 1015
- Howarth, I. D. & Prinja, R. K. 1989, *ApJS*, 69, 527
- Humphreys, R. M. 2010, in *Astronomical Society of the Pacific Conference Series*, Vol. 425, *Hot and Cool: Bridging Gaps in Massive Star Evolution*, ed. C. Leitherer, P. D. Bennett, P. W. Morris, & J. T. Van Loon, 247
- Johansson, S., Zethson, T., Hartman, H., Ekberg, J. O., Ishibashi, K., Davidson, K., & Gull, T. 2000, *A&A*, 361, 977
- Johnson, H. M. & Hogg, D. E. 1965, *ApJ*, 142, 1033
- Johnson, P. G. & Songsathaporn, R. 1981, *MNRAS*, 195, 51
- Kisielius, R., Storey, P. J., Ferland, G. J., & Keenan, F. P. 2009, *MNRAS*, 397, 903
- Kraemer, K. E., Hora, J. L., Egan, M. P., Adams, J., Allen, L. E., Bontemps, S., Carey, S. J., Fazio, G. G., Gutermuth, R., Keto, E., Koenig, X. P., Megeath, S. T., Mizuno, D. R., Motte, F., Price, S. D., Schneider, N., Simon, R., & Smith, H. A. 2010, *AJ*, 139, 2319
- Kwitter, K. B. 1981, *ApJ*, 245, 154
- Lebouteiller, V., Cormier, D., Madden, S. C., Galliano, F., Indebetouw, R., Abel, N., Sauvage, M., Hony, S., Contursi, A., Poglitsch, A., Rémy, A., Sturm, E., & Wu, R. 2012, *A&A*, 548, A91
- López-Sánchez, Á. R. & Esteban, C. 2010, *A&A*, 516, A104
- López-Sánchez, Á. R. & Esteban, C. 2009, *A&A*, 508, 615
- Lozinskaya, T. A. 1970, *Soviet Ast.*, 14, 98
- Luridiana, V., Morisset, C., & Shaw, R. A. 2012, in *IAU Symposium*, Vol. 283, *IAU Symposium*, 422–423
- Maeder, A. 1990, *A&AS*, 84, 139
- Mathis, J. S. & Liu, X.-W. 1999, *ApJ*, 521, 212
- Marston, A. P. 1997, *ApJ*, 475, 188
- Marston, A. P., Chu, Y.-H., & García-Segura, G. 1994a, *apjs*, 93, 229
- Marston, A. P. & Meaburn, J. 1988, *MNRAS*, 235, 391
- Marston, A. P., Yocum, D. R., García-Segura, G., & Chu, Y.-H. 1994b, *apjs*, 95, 151
- Mathis, J. S. 1996, in *Astronomical Society of the Pacific Conference Series*, Vol. 99, *Cosmic Abundances*, ed. S. S. Holt & G. Sonneborn, 327
- McLaughlin, B. M. & Bell, K. L. 2000, *Journal of Physics B Atomic Molecular Physics*, 33, 597
- Mendoza, C. & Zeppen, C. J. 1983, *MNRAS*, 202, 981
- Mesa-Delgado, A. & Esteban, C. 2010, *MNRAS*, 405, 2651
- Mesa-Delgado, A., Esteban, C., García-Rojas, J., Luridiana, V., Bautista, M., Rodríguez, M., López-Martín, L., & Peimbert, M. 2009, *MNRAS*, 395, 855
- Miller, G. J. & Chu, Y.-H. 1993, *apjs*, 85, 137
- Mitra, P. 1991, PhD thesis, Rice Inst., Houston, TX.
- Moore, B. D., Dufour, R. J., Sankrit, R., & Aufdenberg, J. P. 2006, in *Astronomical Society of the Pacific Conference Series*, Vol. 348, *Astrophysics in the Far Ultraviolet: Five Years of Discovery with FUSE*, ed. G. Sonneborn, H. W. Moos, & B.-G. Andersson, 334
- Moore, B. D., Hester, J. J., & Scowen, P. A. 2000, *AJ*, 119, 2991
- Moore, B. D., Walter, D. K., Hester, J. J., Scowen, P. A., Dufour, R. J., & Buckalew, B. A. 2002, *AJ*, 124, 3313
- Nieva, M.-F. & Przybilla, N. 2012, *A&A*, 539, A143
- Noguchi, K., Aoki, W., Kawanomoto, S., Ando, H., Honda, S., Izumiura, H., Kambe, E., Okita, K., Sadakane, K., Sato, B., Tajitsu, A., Takada-Hidai, T., Tanaka, W., Watanabe, E., & Yoshida, M. 2002, *PASJ*, 54, 855
- Oke, J. B. 1990, *AJ*, 99, 1621
- Osterbrock, D. E. & Ferland, G. J. 2006, *Astrophysics of gaseous nebulae and active galactic nuclei* (2nd. ed. Sausalito, CA: University Science Books)
- Palay, E., Nahar, S. N., Pradhan, A. K., & Eissner, W. 2012, *MNRAS*, 423, L35
- Peimbert, M. & Costero, R. 1969, *Boletín de los Observatorios Tonantzintla y Tacubaya*, 5, 3
- Pérez-Montero, E., Hägele, G. F., Contini, T., & Díaz, Á. I. 2007, *MNRAS*, 381, 125
- Podobedova, L. L., Kelleher, D. E., & Wiese, W. L. 2009, *Journal of Physical and Chemical Reference Data*, 38, 171
- Porter, R. L., Ferland, G. J., Storey, P. J., & Detisch, M. J. 2012, *MNRAS*, 425, L28
- . 2013, *MNRAS*, 433, L89
- Quinet, P. 1996, *A&AS*, 116, 573
- Reid, M. J. 1993, *ARA&A*, 31, 345
- Rodríguez, M. 1999, *A&A*, 351, 1075
- Rodríguez, M. & Rubin, R. H. 2005, *ApJ*, 626, 900
- Rola, C. & Pelat, D. 1994, *A&A*, 287, 676
- Rubin, R. H., Simpson, J. P., O'Dell, C. R., McNabb, I. A., Colgan, S. W. J., Zhuge, S. Y., Ferland, G. J. & Hidalgo, S. A. 2011, *MNRAS*, 410, 1320
- Schaerer, D., Contini, T., & Pindao, M. 1999, *A&AS*, 136, 35
- Simón-Díaz, S. & Stasińska, G. 2011, *A&A*, 526, A48
- Stevens, I. R. & Howarth, I. D. 1999, *MNRAS*, 302, 549
- Stock, D. J. & Barlow, M. J. 2010, *MNRAS*, 409, 1429
- Stock, D. J., Barlow, M. J., & Wesson, R. 2011, *MNRAS*, 418, 2532
- Storey, P. J. & Hummer, D. G. 1995, *MNRAS*, 272, 41
- Tayal, S. S. 2011, *ApJS*, 195, 12
- Tayal, S. S. & Zatsarinsky, O. 2010, *ApJS*, 188, 32
- Toalá, J. A. & Arthur, S. J. 2011, *ApJ*, 737, 100
- Treffers, R. R. & Chu, Y.-H. 1982, *ApJ*, 254, 132
- van der Hucht, K. A. 2001, *nar*, 45, 135
- van Leeuwen, F. 2007, *A&A*, 474, 653
- van Marle, A. J., Langer, N., & García-Segura, G. 2005, *A&A*, 444, 837
- . 2007, *A&A*, 469, 941
- Vink, J. S., de Koter, A., & Lamers, H. J. G. L. M. 2001, *A&A*, 369, 574
- Vink, J. S., Gräfener, G., & Harries, T. J. 2011a, *A&A*, 536, L10
- Vink, J. S., Muijres, L. E., Anthonisse, B., de Koter, A., Gräfener, G., & Langer, N. 2011b, *A&A*, 531, A132
- Weaver, R., McCray, R., Castor, J., Shapiro, P., & Moore, R. 1977, *ApJ*, 218, 377
- Wendker, H. J., Smith, L. F., Israel, F. P., Habing, H. J., & Dickel, H. R. 1975, *A&A*, 42, 173
- Wrigge, M., Wendker, H. J., & Wisotzki, L. 1994, *A&A*, 286, 219
- Zhang, H. 1996, *A&AS*, 119, 523